

Effect of quenching rate on the structural and hard magnetic properties of Nd-Fe-B melt-spun ribbons

Cite as: AIP Advances **13**, 025301 (2023); <https://doi.org/10.1063/9.0000524>

Submitted: 03 October 2022 • Accepted: 08 November 2022 • Published Online: 01 February 2023

 Sudeep Singh, Arvindha Babu Diraviam, Rajdeep Sarkar, et al.

COLLECTIONS

Paper published as part of the special topic on [67th Annual Conference on Magnetism and Magnetic Materials](#)

 This paper was selected as an Editor's Pick



View Online



Export Citation



CrossMark

ARTICLES YOU MAY BE INTERESTED IN

[Classification and characterization of coexisting defects from magnetic flux leakage data using deep learning method](#)

AIP Advances **13**, 015029 (2023); <https://doi.org/10.1063/9.0000451>

[High-coercivity heavy-rare-earth-free NdFeB sintered magnets developed by doping \$\text{Ce}_{0.5}\text{Al}_{1.5}\$ and grain boundary diffusion with \$\text{Pr}_{70}\text{Cu}_{15}\text{Al}_{15}\$](#)

AIP Advances **13**, 025226 (2023); <https://doi.org/10.1063/9.0000446>

[Convolutional kernel with \$\text{PrCaMnO}_x\$ -based resistive random-access memory for neuromorphic image processing](#)

AIP Advances **13**, 015318 (2023); <https://doi.org/10.1063/5.0133846>



APL Machine Learning

Machine Learning for Applied Physics
Applied Physics for Machine Learning

**First Articles
Now Online!**

Effect of quenching rate on the structural and hard magnetic properties of Nd-Fe-B melt-spun ribbons

Cite as: AIP Advances 13, 025301 (2023); doi: 10.1063/9.0000524

Submitted: 3 October 2022 • Accepted: 8 November 2022 •

Published Online: 1 February 2023




View Online



Export Citation



CrossMark

Sudeep Singh,^{1,2}  Arvindha Babu Diraviam,² Rajdeep Sarkar,² Arabinda Haldar,^{1,a)} 
and Manivel Raja Muthuvel²

AFFILIATIONS

¹Department of Physics, Indian Institute of Technology Hyderabad, Kandi 502284, Telangana, India

²Defence Metallurgical Research Laboratory, Kanchanbagh, Hyderabad 500058, Telangana, India

Note: This paper was presented at the 67th Annual Conference on Magnetism and Magnetic Materials.

^{a)}Author to whom correspondence should be addressed: arabinda@phy.iith.ac.in

ABSTRACT

The phase structure, microstructure, magnetic and thermomagnetic properties of nanostructured Nd-Fe-B melt-spun ribbons were investigated. The melt-spun ribbons have been prepared at different wheel speeds varying from 17 to 25 m/s. The hard magnetic Nd₂Fe₁₄B phase with (00l) texture, indicating preferred crystallographic orientation, was observed in all the ribbons with some α -Fe(Co) as the minor phase. Nd₂Fe₁₄B grains are uniformly distributed with grain sizes ranging from 50 to 150 nm. A decrease in the average grain size of Nd₂Fe₁₄B and fading away of texture formation in the ribbons were found with the increase in the wheel speeds. The best combination of magnetic properties with a coercivity of 14.5 kOe, the saturation magnetization of 132 emu/g, and the energy product of 16 MGOe was achieved at 23 m/s and these ribbons are suitable for the fabrication of hot deformation Nd-Fe-B magnets.

© 2023 Author(s). All article content, except where otherwise noted, is licensed under a Creative Commons Attribution (CC BY) license (<http://creativecommons.org/licenses/by/4.0/>). <https://doi.org/10.1063/9.0000524>

I. INTRODUCTION

Nd-Fe-B magnets have been widely used in wind turbines, electric vehicles (EVs), and electronic devices in the civilian and defense sectors because of their high magnetic performance. In these magnets, costly and scarce heavy rare-earth elements (HRE), such as Dy or Tb, are added in the sintering route to improve the coercivity.¹⁻⁶ Alternate to the sintering route; the hot-deformation route requires very less HRE and is a promising route to produce these magnets at a low cost. Hot deformed magnets are produced through rapid solidification and hot pressing/deformation techniques.⁷ Nd-Fe-B powder, processed through rapidly solidified ribbons and subsequently crushed, is used as precursors in the hot deformation magnets.⁸⁻¹⁰ Therefore, optimizing rapid solidification parameters is crucial to obtain Nd-Fe-B ribbons with the required grain size, microstructure and desirable hard magnetic properties.¹¹

In the process of producing hot deformed Nd-Fe-B magnets, melt spinning and deformation processes are considered

important steps as the former produces the precursor melt-spun ribbon having the nanograins of Nd₂Fe₁₄B phase with Nd rich phase at the grain boundaries and the later produces the texture resulting in higher coercivity and remanence respectively.⁹⁻¹¹ As the initial phase structure and grain sizes influence the final product's magnetic properties, the melt spinning parameters need to be optimized to get the same.¹²⁻¹⁴ In the melt spinning process, many parameters, such as melt temperature, ejection pressure, wheel speed, nozzle-wheel gap, and nozzle diameter influence the ribbon characteristics.¹²⁻¹⁸ As all parameters affect the dimensions, phases and grain size of the ribbon, wheel speed is the most effective parameter used by most researchers to get the required structure and grain size in the Nd-Fe-B system.^{11,15,16,18} The composition also plays an important role in the hot deformation process. The composition should not only give the required properties but also have the right phase combination to make it deformable. Literature reports that Nd_{13.5}(Fe_{0.975}Co_{0.025})₈₀Ga_{0.5}B₆ alloy yields the highest magnetic properties obtained in the hot deformation process.¹⁹ In

this study, an effort is made to prepare a precursor melt-spun ribbon of $\text{Nd}_{13.6}\text{Fe}_{73.6}\text{Co}_{6.6}\text{Ga}_{0.6}\text{B}_{5.6}$ alloy with the right combination of phases and nano grains through wheel speed variation.

II. METHODS

The nominal composition of $\text{Nd}_{13.6}\text{Fe}_{73.6}\text{Co}_{6.6}\text{Ga}_{0.6}\text{B}_{5.6}$ (at. %) alloy was prepared in a vacuum induction furnace using high purity raw materials (99.9%). The alloy was solidified rapidly to the thin ribbons by a single roller melt spinning unit under an Ar atmosphere in a vacuum chamber with a base pressure of 10^{-2} mbar. Alloy pieces weighing 20 g were kept in the quartz crucible with an internal diameter of 20 mm and an orifice diameter of 0.7 mm. The nozzle tip was positioned 3 mm above the copper wheel with a diameter of 30 cm. The ingot alloy was melted by induction heating using a power of $\sim 5\text{--}10$ kW for 60 seconds, and was then ejected onto the rapidly rotating copper wheel at an ejection temperature of 1400°C . Keeping all the other parameters the same throughout the experiment, only wheel speeds, typically 17–25 m/s, were varied to produce the ribbons having 2–3 mm width with varying thickness. The structure of all the ribbons was analyzed using X-ray diffraction (XRD) using $\text{Co-K}\alpha$ radiation. The diffraction peaks were analyzed and indexed by comparing the JCPDS data of $\text{Nd}_2\text{Fe}_{14}\text{B}$ and the $\alpha\text{-Fe}(\text{Co})$ phase. Scherrer's Equation was used to determine the crystallite size in all ribbons. The microstructure of all the ribbons was studied by transmission electron microscope (TEM). The hard magnetic properties were obtained by a superconducting quantum interference device (SQUID) and thermomagnetic properties were obtained using a vibrating sample magnetometer (VSM).

III. RESULTS AND DISCUSSION

A. Structure and phase analysis of ribbons

The ribbon thickness was found to be 30–50 μm and decrease with the increasing wheel speed. As the flow of the molten alloy through an orifice of quartz crucible is constant due to constant ejection pressure of 2 psi in the melt spinning process, increasing wheel speed causes the molten alloy dragging rate along the copper wheel to increase, thus resulting decrease in thickness. This phenomenon brings about a considerable change in the cooling rate of the molten alloy. As reduced thickness will have low heat content to cool, increasing wheel speed causes an increase in the cooling rate, which may result in reduced grain size expected in this study. Figure 1 shows the XRD pattern of $\text{Nd}_{13.6}\text{Fe}_{73.6}\text{Co}_{6.6}\text{Ga}_{0.6}\text{B}_{5.6}$ ribbons with different wheel speeds, which show that all ribbons exhibit tetragonal $\text{Nd}_2\text{Fe}_{14}\text{B}$ phase (space group $\text{P4}_2\text{mnm}$) as a major phase and $\alpha\text{-Fe}(\text{Co})$ phase as a minor phase. It is found that the $\langle 001 \rangle$ family planes show increased intensity as compared to other peaks of $\text{Nd}_2\text{Fe}_{14}\text{B}$ phase, which signifies a strong texture formation along $\langle 001 \rangle$ direction in all ribbons. Note here that the texture formation is more prominent on the exposed side of the ribbon as compared to the wheel side. The increase in wheel speed reduces the intensity of texture, as can be seen from the reduced relative intensity of $\langle 001 \rangle$ family plane peaks as compared to other peaks of $\text{Nd}_2\text{Fe}_{14}\text{B}$ phase. The texture formation in the melt-spun ribbon is due to the cooling rate gradient achieved along the thickness of the ribbon during the melt-spinning process. In melt spinning during the ribbon formation, the heat is extracted mainly into the copper wheel through

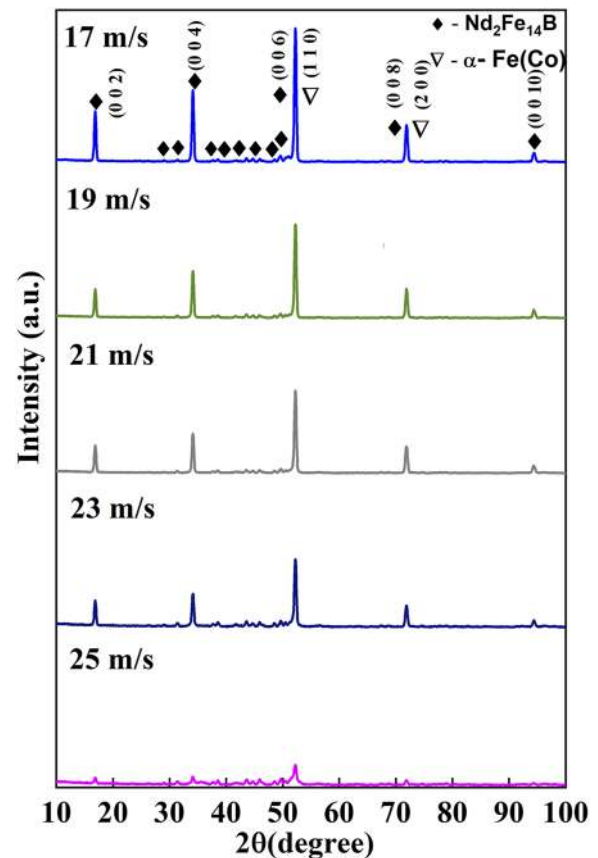


FIG. 1. XRD pattern of the Nd–Fe–B melt-spun ribbons produced at different wheel speeds.

the ribbon side touching the wheel and the on the other opposite side, the heat loss is only due to convection which is very minimal considering the partial Ar atmosphere equipment chamber, and this results in cooling rate gradient along the thickness of the ribbon. Hence, nucleation starts at the point of highest cooling rate, i.e., at the wheel side of the ribbon, and grows along the direction perpendicular to the thickness as the grains, generally, grow along the minimum energy direction, i.e., the $\langle 001 \rangle$ crystallographic direction which is in the opposite direction of the heat extraction. The mean crystallite size of the $\text{Nd}_2\text{Fe}_{14}\text{B}$ phase, calculated using the Scherrer formula, is $\sim 30\text{--}50$ nm for all the ribbons while increasing the wheel speed decreases the mean crystallite size. The crystallite sizes at the wheel sides are less than that of the air sides.

B. Microstructure

The cross-sectional microstructures of ribbons obtained through a scanning electron microscope (SEM) (not shown here) show that all ribbons show columnar grains. As discussed earlier, the columnar grains result from the texture formation happening due to the thermal gradient along the thickness during the melt spinning experiment. Figures 2(a)–2(e) shows the TEM bright field (BF) micrographs of melt-spun ribbons processed at different wheel

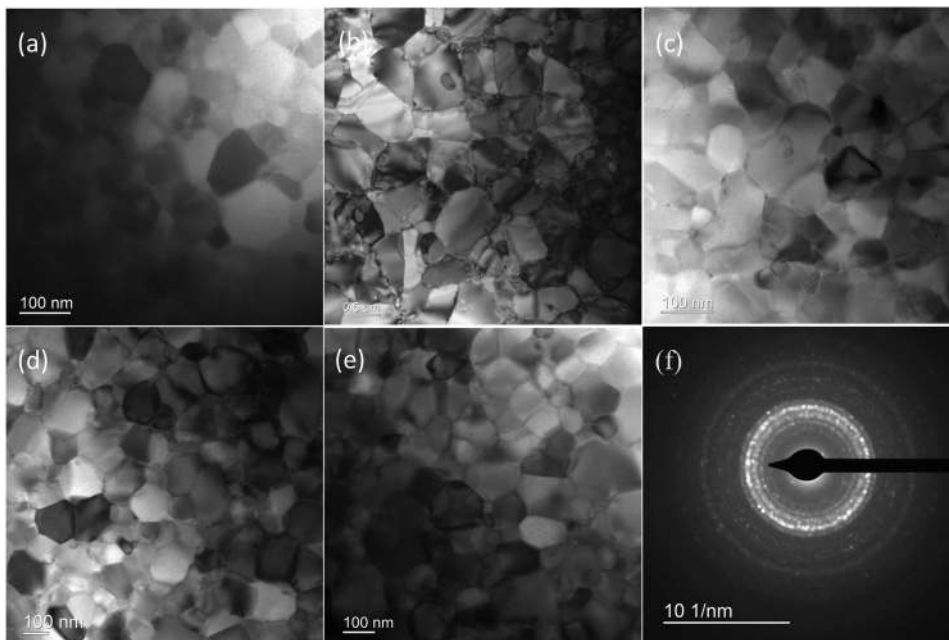


FIG. 2. TEM Image of melt-spun ribbons produced at a wheel speed of (a) 17 m/s (b) 19 m/s (c) 21 m/s (d) 23 m/s (e) 25 m/s and (f) SAED pattern of melt spun-ribbon produced at a wheel speed of 21 m/s.

speeds, and (f) corresponds to the selected area electron diffraction (SAED) pattern of ribbon processed at 21 m/s. TEM BF micrographs reveal that the grains are equiaxed in nature with the grain size ranging from 50 to 150 nm. Since the grains are in the nano range, the SAED pattern could not be taken; hence, identifying grains corresponding to $\text{Nd}_2\text{Fe}_{14}\text{B}$ phase and $\alpha\text{-Fe}(\text{Co})$ phase through the SAED pattern was not possible. However, the ring SAED pattern obtained from the 21 m/s wheel speed ribbon showed the existence of both phases. A careful examination of the grain boundary in many grains shows a different contrast compared to the grains, which signifies the formation of Nd rich phase as reported in many of the

previous reports.^{20,21} Note that the Nd-rich phase has a low melting point and plays an important role in the hot deformation process by melting and assisting the texture formation. However, this phase fraction is extremely low, which will form in high fractions during further processing, such as hot compression and hot deformation.

C. Magnetic properties

Figure 3(a) shows the magnetization vs temperature (M vs T) plots of all the ribbons obtained at the applied field (H) of 500 Oe. There is a sharp drop in magnetization values at two temperatures around 380°C and $770\text{--}800^\circ\text{C}$ in the M vs T curves for all

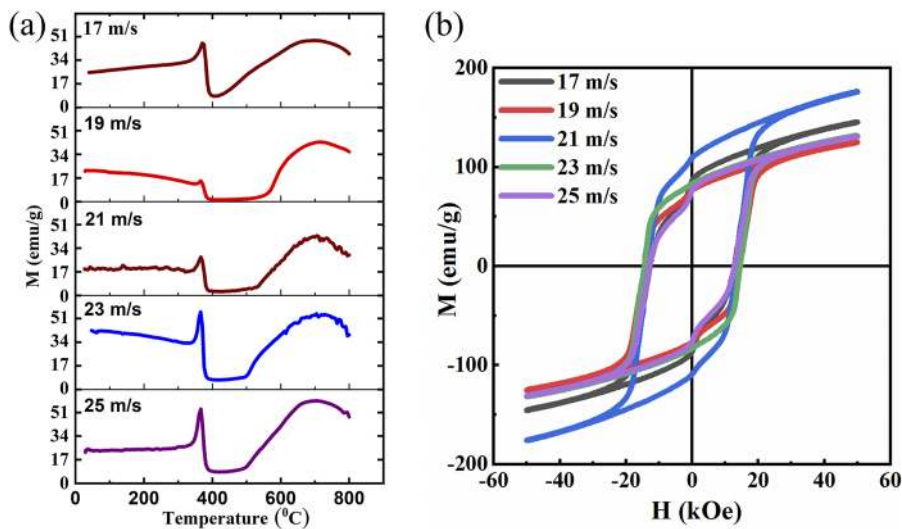


FIG. 3. MT curves (a) and Hysteresis loop (b) of the Nd-Fe-B melt-spun ribbons produced at different wheel speeds.

the ribbons, which can be assigned to ferromagnetic to paramagnetic transition (Curie temperature, T_C) of $\text{Nd}_2\text{Fe}_{14}\text{B}$ and $\alpha\text{-Fe}(\text{Co})$ phases, respectively. The magnetization shows an increasing trend at around 400°C – 550°C in all the ribbons. This may correspond to either precipitation of the α -iron phase during the heating of the sample or the rejection of the other elements, such as Nd, B and Ga, from the $\alpha\text{-Fe}(\text{Co})$ phase. In addition to the drop in magnetization around T_C , a sharp increase in magnetization before the drop can be observed in ribbons, which is related to the strong anisotropy of $\text{Nd}_2\text{Fe}_{14}\text{B}$ phase. As only minor loops could be obtained using the VSM, the M-H loops were obtained using SQUID-VSM at the maximum applied field of 50 kOe. Figure 3(b) shows the hysteresis loop of all the melt-spun ribbons. It is found that the ribbons are well saturated, and the hysteresis loops show two-step behavior except for the ribbon prepared at 23 m/s wheel speed. This behavior can be attributed to the presence of two phases. i.e., $\text{Nd}_2\text{Fe}_{14}\text{B}$ and the $\alpha\text{-Fe}(\text{Co})$ phases. It is to note that the step is observed near the y-axis, which means the step arises from the low coercivity phase, i.e., $\alpha\text{-Fe}(\text{Co})$ phase, which is a soft magnetic phase. The step height decreases as the wheel speed increases and finally vanishes at 23 m/s, which means that the volume fraction of the $\alpha\text{-Fe}(\text{Co})$ phase decreases continuously and finally vanishes at 23 m/s. The step again re-appears with a further increase in wheel speed to 25 m/s, which signifies the contribution of the $\alpha\text{-Fe}(\text{Co})$ phase. The coercivity (H_c) of as-melt-spun ribbons varies from 12.8 to 14.5 kOe. It shows an increasing trend with wheel speed and peaks at 23 m/s and then decreases at higher wheel speed, i.e., 25 m/s. Regarding the two-step behavior of the M-H loops, the coercivity of the melt-spun ribbons is influenced by the presence of the $\alpha\text{-Fe}(\text{Co})$ phase and its volume fraction. The maximum coercivity is observed at 23 m/s wheel speed; coincidentally, the two-step behavior vanishes at this wheel speed. This both signifies the presence of a very low volume fraction or almost nil fraction of the $\alpha\text{-Fe}(\text{Co})$ phase in 23 m/s wheel speed, and it also suggests the importance of phase control during the melt spinning process. The grain size influence on the coercivity also cannot be ruled out as the grain size decreases with increasing wheel speed which we have also observed. The change in volume fraction of the $\alpha\text{-Fe}(\text{Co})$ phase can be explained in terms of the Nd content which is slightly above the line composition of the $\text{Nd}_2\text{Fe}_{14}\text{B}$ phase and it leads to a peritectic reaction when the liquid alloy is solidified during melt spinning. In this peritectic reaction, the molten liquid (L) is transformed into $L + \alpha\text{-Fe}(\text{Co})$ and the liquid thus formed further gets transformed into $\delta\text{-Nd}_2\text{Fe}_{14}\text{B}$, $\eta\text{-Nd}_{1.1}\text{Fe}_4\text{B}_4$ and Nd-rich phases through further peritectic and eutectic reactions. Depending on the cooling rate, the volume fraction of the $\alpha\text{-Fe}(\text{Co})$ phase changes and, in particular, an increase in the cooling rate leads to the reduced fraction of the $\alpha\text{-Fe}(\text{Co})$ phase because of the quick passing over of the solidifying alloy through the peritectic region. In the present study too increasing wheel speed (increasing cooling rate), led to the formation of a reduced $\alpha\text{-Fe}(\text{Co})$ phase with complete suppression of the $\alpha\text{-Fe}(\text{Co})$ phase at 23 m/s wheel speed. The re-appearance of the $\alpha\text{-Fe}(\text{Co})$ phase at higher wheel speeds may be caused by the decreasing cooling rate because of the low residing time of the melt-spun ribbon on the Cu wheel due to high centrifugal force at high wheel speeds. The volume fraction of the $\alpha\text{-Fe}(\text{Co})$ phase could not be estimated due to the nano size of the grains and overlapping XRD peaks. The present study suggests that the melt-spun ribbon processed at 23 m/s with the coercivity (H_c) of 14.5 kOe, saturation

magnetization (M_s) of 132 emu/g, and maximum energy product $(\text{BH})_{\text{max}}$ of 16 MGOe will be a suitable precursor ribbon for further processing of hot press and hot deformation.

IV. CONCLUSIONS

In the present study, an effort was made to prepare precursor melt-spun Nd-Fe-B ribbons which will be further used to prepare hot deformed Nd-Fe-B magnets. Initially, $\text{Nd}_{13.6}\text{Fe}_{73.6}\text{Co}_{6.6}\text{Ga}_{0.6}\text{B}_{5.6}$ ribbons were prepared by melt spinning technique at different wheel speeds ranging from 17 to 25 m/s. Melt-spun ribbons form $\text{Nd}_2\text{Fe}_{14}\text{B}$ and $\alpha\text{-Fe}(\text{Co})$ phases with grain sizes varying from 50 to 150 nm. All ribbons are found to show two transitions corresponding to Curie temperatures of $\text{Nd}_2\text{Fe}_{14}\text{B}$ and $\alpha\text{-Fe}(\text{Co})$ phases. The presence of the $\alpha\text{-Fe}(\text{Co})$ phase influences the hysteresis loop to exhibit two-step behavior and coercivity. This study suggests that the ribbon prepared at the wheel speed of 23 m/s with the coercivity of 14.5 kOe, the saturation magnetization of 132 emu/g, and the maximum energy product $(\text{BH})_{\text{max}}$ of 16 MGOe will be a suitable precursor ribbon for further processing of hot press and hot deformation.

ACKNOWLEDGMENTS

The use of the facilities of the Defense Metallurgical Research Laboratory (DMRL), DRDO, is gratefully acknowledged.

AUTHOR DECLARATIONS

Conflict of Interest

The authors have no conflicts to disclose.

Author Contributions

Sudeep Singh: Conceptualization (equal); Data curation (equal); Formal analysis (equal); Investigation (equal); Methodology (equal); Software (equal); Validation (equal); Visualization (equal); Writing – original draft (equal); Writing – review & editing (equal). **Arvindha Babu Diraviam:** Conceptualization (equal); Formal analysis (equal); Investigation (equal); Resources (equal); Supervision (equal); Validation (equal); Visualization (equal); Writing – review & editing (equal). **Rajdeep Sarkar:** Resources (equal); Software (equal). **Arabinda Haldar:** Conceptualization (equal); Funding acquisition (equal); Methodology (equal); Project administration (equal); Resources (equal); Software (equal); Supervision (equal); Validation (equal); Visualization (equal); Writing – review & editing (equal). **Manivel Raja Muthuvel:** Conceptualization (equal); Methodology (equal); Project administration (equal); Resources (equal); Supervision (equal); Validation (equal); Visualization (equal); Writing – review & editing (equal).

DATA AVAILABILITY

The data that support the findings of this study are available from the corresponding author upon reasonable request.

REFERENCES

- ¹H. W. Chang, G. T. Lin, Y. J. Wong, W. M. Huang, and W. C. Chang, *AIP Adv.* **11**, 025001 (2021).
- ²Y. J. Wong, H. W. Chang, Y. I. Lee, W. C. Chang, C. H. Chiu, and C. C. Mo, *J. Magn. Magn. Mater.* **515**, 167287 (2020).
- ³Y. I. Lee, G. Y. Huang, S. T. Chang, C. W. Shih, W. C. Chang, H. W. Chang, and Y. J. Chen, *IEEE Trans. Magn.* **8**, 1 (2017).
- ⁴Y. I. Lee, Y. J. Wong, H. W. Chang, and W. C. Chang, *J. Magn. Magn. Mater.* **478**, 43 (2019).
- ⁵S. Fu, M. Yan, J. Jin, H. Nagata, and J. Xie, *Mater. Lett.* **283**, 128718 (2021).
- ⁶T. Zhou, P. Qu, W. Pan, R. Liu, M. Li, S. U. Rehman, Z. Zhong, and G. Xie, *J. Alloys Compd.* **856**, 158191 (2020).
- ⁷K. Hioki, *Sci. Technol. Adv. Mater.* **22**, 72 (2021).
- ⁸Z. W. Liu, H. Y. Huang, X. X. Gao, H. Y. Yu, X. C. Zhong, J. Zhu, and D. C. Zeng, *J. Phys. D: Appl. Phys.* **44**, 025003 (2011).
- ⁹Y. H. Hou, Y. L. Huang, Z. W. Liu, D. C. Zeng, S. C. Ma, and Z. C. Zhong, *Mater. Sci. Eng. B Solid-State Mater. Adv. Technol.* **178**, 990 (2013).
- ¹⁰Z. W. Liu, Y. L. Huang, H. Y. Huang, X. C. Zhong, H. Y. Yu, and D. C. Zeng, *Key Eng. Mater.* **510-511**, 307 (2012).
- ¹¹C. Rong and B. Shen, *Chinese Phys. B* **27**, 117502 (2018).
- ¹²K. P. Su, Z. W. Liu, D. C. Zeng, D. X. Huo, L. W. Li, and G. Q. Zhang, *J. Phys. D: Appl. Phys.* **46**, 245003 (2013).
- ¹³A. Manaf, M. Al-Khafaji, P. Z. Zhang, H. A. Davies, R. A. Buckley, and W. M. Rainforth, *J. Magn. Magn. Mater.* **128**, 307 (1993).
- ¹⁴A. Manaf, R. A. Buckley, and H. A. Davies, *J. Magn. Magn. Mater.* **128**, 302 (1993).
- ¹⁵T. Saito, *J. Alloys Compd.* **505**, 23 (2010).
- ¹⁶V. I. Tkatch, A. I. Limanovskii, S. N. Denisenko, and S. G. Rassolov, *Mater. Sci. Eng. A* **323**, 91 (2002).
- ¹⁷A. Manaf, M. Leonowicz, H. A. Davies, and R. A. Buckley, *Mater. Lett.* **13**, 194 (1992).
- ¹⁸S. P. H. Marashi, A. Abedi, S. Kaviani, S. H. Aboutalebi, M. Rainforth, and H. A. Davies, *J. Phys. D: Appl. Phys.* **42**, 115410 (2009).
- ¹⁹T. Saito, M. Fujita, T. Kuji, K. Fukuoka, and Y. Syono, *J. Appl. Phys.* **83**, 6390 (1998).
- ²⁰G. Shi, Z. Wang, X. Bai, W. Yan, Y. Luo, and D. Yu, *J. Rare Earths* **38**, 1312 (2020).
- ²¹F. Chen, *J. Magn. Magn. Mater.* **514**, 167227 (2020).